

Anisotropy of the irreversibility field for Zr-doped (Y,Gd)Ba₂Cu₃O_{7-x} thin films up to 45T

C. Tarantini¹, J. Jaroszynski¹, F. Kametani¹, Y. L. Zuev^{2,3}, A. Gurevich^{1,4}, Y. Chen⁵,

V. Selvamanickam⁶, D. C. Larbalestier¹, D. K. Christen²

¹National High Magnetic Field Laboratory, Florida State University, Tallahassee, Florida 32310, USA

²Oak Ridge National Laboratory, Oak Ridge, Tennessee 37831, USA

³University of Tennessee, Knoxville, Tennessee 37996, USA

⁴Department of Physics, Old Dominion University, Norfolk, Virginia 23529, USA

⁵SuperPower Inc., Schenectady, New York 12304, USA

⁶Department of Mechanical Engineering and the Texas Center for Superconductivity,

University of Houston, Houston, Texas 77204, USA

The anisotropic irreversibility field B_{Irr} of two YBa₂Cu₃O_{7-x} thin films doped with additional rare earth (RE)=(Gd,Y) and Zr and containing strong correlated pins (splayed BaZrO₃ nanorods, and RE₂O₃ nanoprecipitates), has been measured over a very broad range up to 45T at temperatures $56\text{ K} < T < T_c$. We found that the experimental angular dependence of $B_{Irr}(\theta)$ does not follow the mass anisotropy scaling $B_{Irr}(\theta) = B_{Irr}(0)(\cos^2\theta + \gamma^{-2}\sin^2\theta)^{-1/2}$, where $\gamma = (m_c/m_{ab})^{1/2} = 5-6$ for the RE-doped YBa₂Cu₃O_{7-x} (REBCO) crystals, m_{ab} and m_c are the effective masses along the ab plane and the c -axis, respectively, and θ is the angle between \mathbf{B} and the c -axis. For \mathbf{B} parallel to the ab -planes and to the c -axis correlated pinning strongly enhances B_{Irr} , while at intermediate angles, $B_{Irr}(\theta)$ follows the scaling behavior $B_{Irr}(\theta) \propto (\cos^2\theta + \gamma_{RP}^{-2}\sin^2\theta)^{-1/2}$ with the effective anisotropy factor $\gamma_{RP} \approx 3$ significantly smaller than the mass anisotropy would suggest. In spite of the strong effects of c -axis BaZrO₃ nanorods, we found even greater enhancements of B_{Irr} for fields along the ab -planes than for fields parallel to the c -axis, as well as different temperature dependences of the correlated pinning contributions to B_{Irr} for $B//ab$ and $B//c$. Our results show that the dense and strong pins, which can now be incorporated into REBCO thin films in a controlled way, exert major and diverse effects on the measured vortex pinning anisotropy and the irreversibility field over wide ranges of B and T . In particular, we show that the relative contribution of correlated pinning to B_{Irr} for $B//c$ increases as the temperature increases due to the suppression of thermal fluctuations of vortices by splayed distribution of BaZrO₃ nanorods.

I. INTRODUCTION

In recent years the properties of $\text{YBa}_2\text{Cu}_3\text{O}_{7-x}$ (YBCO), or more generally any rare-earth- (RE-) doped $\text{YBa}_2\text{Cu}_3\text{O}_{7-x}$ (REBCO) thin films, have been progressively improved by mitigating the grain boundary limitation of the critical current density J_c and by increasing the vortex pinning by incorporating non-superconducting nanoparticles or nanorods. Pure YBCO exhibits an upper critical field anisotropy $\gamma = B_{c2}^{(ab)}/B_{c2}^{(c)} = (m_c/m_{ab})^{1/2}$ of 5-6, where m_c/m_{ab} is the mass anisotropy ratio $\sim 25-36$. The substitution of RE on the Y site (or the enrichment of Y or RE) produces RE_2O_3 nanoparticle^{1,2,3} pinning centers while the addition of Zr induces self-assembled BaZrO_3 (BZO) nanorods able to strongly increase J_c for $B//c$.^{1,2,4} Blatter's scaling approach⁵ for weak isotropic random pinning (RP) has often been used^{6,2} to separate the RP contribution to the angular dependence of J_c determined by the mass anisotropy from the contributions of correlated pins which are most pronounced for the magnetic fields parallel to the ab -planes or to the c -axis. The scaling approach⁵ enables one to calculate the angular dependence of $J_c(H, \theta)$ by rescaling the field dependence of $J_c(H)$ for $B//c$ according to $B \rightarrow B\varepsilon_\theta$ where $\varepsilon_\theta = (\cos^2\theta + \gamma^{-2} \sin^2\theta)^{1/2}$. Here $\gamma = (m_c/m_{ab})^{1/2} = 5-6$ for the REBCO, m_{ab} and m_c are the effective masses along the ab plane and the c -axis, respectively, and θ is the angle between \mathbf{B} and the c -axis. This approach works well for clean YBCO films with weak correlated pinning where $\gamma \sim 5$ is actually found.⁷ However, for films with high density of c -axis aligned nanorods (like BZO), the angular dependence of J_c for the fields tilted away from the symmetry axis was found to follow the scaling behavior with $\varepsilon_\theta = (\cos^2\theta + \gamma_{\text{eff}}^{-2} \sin^2\theta)^{1/2}$ and the anisotropy parameter γ_{eff} smaller than γ .^{2,6} Such reduced anisotropy was ascribed by the authors to the effect of strong RP after the effect of correlated pinning has been separated from the angular dependence of J_c .

The complex effects of strong random and correlated pinning on the angular dependence of the irreversibility field B_{Irr} and particularly, the question if the contributions of random and correlated

pinning on $B_{Irr}(\theta)$ can be identified from the observed angular dependence $B_{Irr}(\theta)$ are not well understood. This is not an easy task because the relative weights of random and correlated contributions can change as the temperature decreases and the role of thermal fluctuations of vortices diminishes. In turn, the observation of these changes also requires measurements of $B_{Irr}(\theta)$ at very high magnetic fields, which was the main goal of this work. Because the irreversibility field B_{Irr} at low temperatures becomes much larger than the matching field, B_ϕ , of the artificially introduced defects (seldom greater than 3-5 T), B_{Irr} might be less affected by the correlated pinning than J_c , making it easier to reveal the effect of strong RP on B_{Irr} . This is the central conjecture of this paper, in which we present the angular dependence of B_{Irr} performed in very high dc fields up to 45 T. Access to such high fields allows us to conduct B_{Irr} measurements down to temperatures of 56 K where thermal fluctuations weaken and the pinning behavior starts to change. We show that such high fields allow us to see that multiple different effects are present in B_{Irr} and to check how the effective anisotropy of B_{Irr} differs from the mass anisotropy. In particular, we found that the angular dependence $B_{Irr}(\theta)$ for the intermediate field orientations not too close to the symmetry axis approximately follows the scaling behavior $B_{Irr}(\theta) = B_{Irr}(0)(\cos^2\theta + \gamma_{RP}^{-2} \sin^2\theta)^{-1/2}$ with the effective anisotropy parameter $\gamma_{RP} \approx 3$, significantly smaller than the mass anisotropy $\gamma = 5-6$ for REBCO. This behavior of $B_{Irr}(0)$ appears qualitatively similar to the angular dependence of $J_c(\theta)$ discussed above, although the parameters γ_{eff} and γ_{RP} may be different. Moreover, we were also able to identify and measure the strength of the correlated pinning contribution to B_{Irr} that appears to be particularly effective for $B//ab$ and for $B//c$ at temperatures close to the critical temperature, T_c . We also investigated the behavior of the electrical resistance $R(B) \propto (B - B_{Irr})^s$ near the depinning transition by studying the critical exponents s and the way that the pinning mechanisms change with temperature. Finally we compare our results with those

previously reported in underdoped single crystals,⁸ optimally doped thin films⁹ and thin films of REBCO containing additional pinning centers.¹⁰

II. EXPERIMENTAL RESULTS AND ANALYSIS

The samples studied in this work are $\sim 1\text{-}\mu\text{m}$ -thick and $\sim 0.5\text{-}\mu\text{m}$ -thick (Gd,Y)BCO thin films, both made with additional Zr and rare earth (RE). The superconducting films were deposited by metal organic chemical vapor deposition (MOCVD) on Ion Beam Assisted Deposition (IBAD)-MgO template, which has a multilayer structure of LaMnO₃/homoepitaxial-MgO/IBAD-MgO/Y₂O₃/Al₂O₃/Hastelloy tape. The growth process of such samples has been described previously.³ Here, compositions of the liquid precursors delivered for MOCVD deposition of the two samples were Zr_{0.1}Gd_{0.66}Y_{0.66}Ba₂Cu₃ and Zr_{0.05}Gd_{0.65}Y_{0.65}Ba₂Cu₃ identified in the following as 10%Zr-REBCO (1 μm) and 5%Zr-REBCO (0.5 μm). The films have a critical temperature of 90.2 and 91.0 K, respectively. The microstructure of 5%Zr-REBCO was examined in a JEOL JEM2011 transmission electron microscope (TEM). As was previously reported¹⁻⁴, the Zr and RE additions greatly enhance vortex pinning by introducing nanoprecipitates and nanorods in the REBCO matrix as shown in the transverse cross-sectional TEM images of Fig.1. Figure 1(a) shows the entire thickness of the 5%Zr-REBCO film in which three different pinning defects can be seen. The contrasts of vertical dark rods, black dots and horizontal white lines represent the BZO nanorods, RE₂O₃ nano-precipitates and stacking faults, respectively, all of which are distributed quite uniformly in the REBCO matrix. The BZO nanorods form in a splayed manner,⁴ but with a statistically averaged angle between the direction of nanorods and the REBCO *ab*-planes of approximately 80° rather than being 90°, as indicated in the high resolution TEM (HREM) image of Fig. 1(b). In addition to the $\sim 5\text{-nm}$ -diameter BZO nanorods, Fig. 1(b) also shows a high density of stacking faults with an average spacing of $\sim 10\text{ nm}$ and RE₂O₃ nanoprecipitates that are $\sim 6\text{ nm}$ thick and $\sim 7\text{ nm}$ in diameter. HREM imaging of the interface between the REBCO and the buffer

revealed that the REBCO *ab*-planes are not parallel to, but are tilted $\sim 3^\circ$ from the interface and thus the film surface [Fig. 1(c)]. TEM imaging previously performed on the 10%Zr-REBCO sample showed a similar microstructure, although with a larger density of RE₂O₃ precipitates arranged in a plane slightly tilted from the *ab* planes.¹¹

The angular dependent transport measurements were performed in a Quantum Design 16 T Physical Property Measurement System (PPMS) and in a 31 T resistive and a 45 T hybrid dc magnets at the National High Magnetic Field Laboratory (NHMFL). Electrical resistivity measurements were made using a four-wire, ac resistance bridge at a current density of $<100 \text{ A/cm}^2$, with the magnetic field applied perpendicular to the current in a maximum Lorentz force configuration. Measurements were made in ramped field, constant-temperature mode, with the irreversibility field defined at 1% of the normal state resistance just above the superconducting transition. The angular dependencies of $B_{Irr}(\theta)$ are shown in Fig. 2 as filled (PPMS data) and empty (high dc field data) symbols where θ is the angle between the field and the *c*-axis (the field alignment with the main crystallographic axes was determined by fits of the RP contribution to $B_{Irr}(\theta)$, but not relatively to the tape axes, as explained later). All the data show marked peaks close to 90° and 270° , where the field is aligned with the *ab* plane and an intermediate, almost flat region which has a small peak at about 190° . This almost flat region is $\sim 80^\circ$ - 90° wide at higher temperatures, but narrows to $\sim 40^\circ$ with decreasing temperature.

The angular dependency of the irreversibility field $B_{Irr}(\theta)$ is strongly affected by the sample nanostructure, as was found also for $J_c(\theta)$.⁴ However, at high magnetic fields ($B \gg B_\phi$, where $B_\phi \leq 5 \text{ T}$), the contribution of the *c*-axis-correlated pinning effects becomes less pronounced, and therefore the correlation of angular dependence with the REBCO mass anisotropy in B_{Irr} should become more explicit than in the critical current measurements. In order to analyze $B_{Irr}(\theta)$ we have to take into account different contributions that may affect its behavior. The irreversibility field in the presence of weak RP roughly scales like the vortex melting field which mainly depends on the mass anisotropy.⁵

Thus, to separate the RP contribution $B_{Irr,RP}$ in the observed $B_{Irr}(\theta) = B_{Irr,cor} + B_{Irr,RP}$ we use a scaling expression for $B_{Irr,RP}(\theta)$ similar to the one for the melting field,⁵ but assuming that the effective anisotropy parameter γ_{RP}^2 might differ from $\gamma^2 \approx 25 - 36$

$$B_{Irr,RP}(\theta) = \frac{B_{Irr}(0)}{\sqrt{\cos^2(\theta) + \gamma_{RP}^{-2} \sin^2(\theta)}} = \frac{B_{Max}}{\sqrt{\sin^2(\theta) + \gamma_{RP}^2 \cos^2(\theta)}} \quad (1)$$

with $B_{Max} = \gamma_{RP} B_{Irr}(0)$. The question to be addressed is then how the correlated pinning defect nanostructure of the REBCO thin films would affect the angular dependence of B_{Irr} . Columnar BZO nanorods produce strong correlated pinning for the field nearly parallel to the c -axis direction affecting the region around 180° in Fig. 2. Planar second-phase defects, stacking faults and the intrinsic pinning by the REBCO layered structure can give additional pinning contributions for fields parallel to the ab planes that are slightly misoriented from the direction of the surface because of the $\sim 3^\circ$ tilted REBCO planes [Fig 1(c)]. The data in Fig. 2 clearly show all these contributions.

To deconvolute different correlated pinning contributions causing deviations of the observed $B_{Irr}(\theta)$ from the $B_{Irr,RP}(\theta)$ scaling, we rewrite Eq. (1) as follows

$$\frac{1}{B_{Irr,RP}^2(\theta)} = \frac{1}{B_{Max}^2} + \frac{\gamma_{RP}^2 - 1}{B_{Max}^2} \cos^2(\theta) \quad (2)$$

This form is convenient because correlated pinning contributions to $B_{Irr}(\theta)$ on top of the RP component would manifest themselves as deviations of $1/B_{Irr}^2(\theta)$ plotted as a function of $\cos^2\theta$ from a straight line. Figure 3 shows an example of this approach using the replotted data from Fig. 2 (10%Zr-REBCO at 72.6 K). At intermediate orientations between $B//c$ and $B//ab$ a good fit to Eq.2 can be clearly seen, while there are deviations for $\cos^2(\theta)$ close to 0 and 1 due to the correlated pinning contributions. These RP contributions to $B_{Irr}(\theta)$ are shown in Fig. 2 as continuous lines for which the parameters B_{Max} and γ_{RP} have been estimated from the best fits to Eq. (2) for every data series. This

analysis yields for both samples $\gamma_{RP} \sim 3$, which is smaller than $\gamma = 5-6$ for REBCO single crystals. Possible reasons for the reduced anisotropy parameter γ_{RP} will be discussed below. Because of the different temperature and field ranges over which the two samples were characterized, in the following we mainly focus on the c -axis peak of 5%Zr-REBCO (measured down to 56K) and on the ab peak of 10%Zr-REBCO, which was better characterized in the 45T magnet.

Close inspection shows that the experimental data in Fig. 2 deviate from the continuous line in an asymmetric way in the regions indicated by the arrows in the inset of Fig. 2(a) for 10%Zr-REBCO, whereas there is no appreciable asymmetry for 5%Zr-REBCO [see 77K data in Fig. 2(b)]. Such asymmetry indicates the presence of correlated pinning not perfectly aligned with the ab planes of 10%Zr-REBCO. Subtracting the RP contribution to the experimental data, we extract the correlated pinning contributions $\Delta B_{Irr}(\theta) = B_{Irr}(\theta) - B_{Irr,RP}(\theta)$ that are shown in Fig. 4. The most pronounced effect of correlated pinning is that B_{Irr} along the ab planes is strongly enhanced from 20 to 45 T at 78 K, more than doubling the expected RP component of B_{Irr} . The inset of Fig. 4(a) shows that the shape of the ab -peak for the 10%Zr-REBCO sample becomes cusp-like on decreasing the temperature from 84K to 78K. This effect is emphasized in the inset of Fig. 5 where the $\Delta B_{Irr}(\theta)$ data are plotted on a logarithmic scale. Here all the curves for $T > 78K$ follow the same behavior, but $B_{Irr}(78K)$ clearly has a double structure consisting of wide and narrow peaks. The inset of Fig. 4(a) (continuous lines) shows that the high temperature data can be described by a single Lorentzian peak [full width half maximum (FWHM) $\sim 12^\circ$], whereas the 78K data exhibit a superposition of two Lorentzian peaks (the light blue curves). The sharper (FWHM $\sim 1.6^\circ$) and the most intense peak is aligned with the ab plane, while the wider (FWHM $\sim 12^\circ$) and weaker one is slightly shifted to the low-angle side, as already noted in Fig. 2a. Normalizing the ab -peak-correlated pinning to the RP contribution (Fig. 5, main panel), we observe that the wider peak becomes stronger at high temperatures, while the narrower one emerges only at low

temperatures, clearly suggesting different mechanisms that affect B_{Irr} . The narrower peak seems not to be detected below 78K but this may be because B_{Irr} close to ab is beyond the 45T limit of our measurements.

For fields nearly parallel to the c -axis, the inset of Fig. 4(b) shows the peaks of ΔB_{Irr} for the 5%Zr-REBCO sample. The peak magnitude increases with decreasing temperature and its position, which at higher temperatures is at over 190° , moves closer to 180° at lower temperatures. However, the ΔB_{Irr} data normalized to the RP contribution indicate that the relative contribution of the correlated pinning decreases at lower temperature (Fig. 6), a result that is different from what we found for the ab -plane peak. In the 10%Zr-REBCO, the higher Zirconium content does not appear to have a positive effect on the c -axis pinning contribution to B_{Irr} . The reason can be related to the fact that, in this relatively high-temperature regime, the irreversibility field is reduced due to the slightly suppressed critical temperature of 10%Zr-REBCO.

III. DISCUSSION

A. Random pinning

The effective anisotropy parameter $\gamma_{RP} \approx 3$ experimentally found for the intermediate range of field orientations far from the main crystallographic axes, is significantly lower than the mass anisotropy parameter $\gamma \approx 5 - 6$. This reduced value of γ_{RP} indicates the effect of RP on B_{Irr} . Here several mechanisms affecting the $B_{Irr}(\theta)$ can be identified. For weak pinning by randomly distributed point defects, B_{Irr} is defined by the condition $U(B_{Irr}, T) \sim k_B T$ where U is the activation barrier which determines the electric field $E \propto J \rho_n \exp [-U/k_B T]$ due to thermally activated hopping of vortices. In the scaling approach, $U(B_{Irr}, T)$ depends only on the product $B \varepsilon_\theta$ where $\varepsilon_\theta = (\cos^2 \theta + \gamma^2 \sin^2 \theta)^{1/2}$ and θ is the

angle between the c -axis and \mathbf{B} . This results in Eq. (1) in which the magnitude B_{Max} depends on the pinning strength.⁵

The actual structure of randomly distributed pinning nanoprecipitates can change the scaling angular dependence of $B_{Irr,RP}$ due to (1) shape anisotropy of nanoprecipitates, (2) anisotropy of core and magnetic interaction of a vortex with nanoprecipitates, (3) different mean spacing between the precipitates in the ab planes and along the c -axis. For instance, the magnetic interaction force f_p of a vortex with a round precipitate is anisotropic so that $f_p(B//c) \approx \gamma f_p(B//ab)$, reflecting the decrease of screening currents in a vortex upon rotating toward the ab plane. In turn, the reduction of both f_p and the line tension of a vortex parallel to the ab planes have opposite effects on J_c ⁶ and can also result in a weaker angular dependence of $B_{Irr}(\theta)$ as compared to what is expected from the effective mass anisotropy only. Moreover, oblate nanoprecipitates can enhance pinning of vortices parallel to the ab plane, making $f_p(B//ab)$ larger than $f_p(B//c)$ if the aspect ratio of precipitates is greater than γ . Thus the observed reduction of γ_{RP} can result from multiple conflicting mechanisms of pinning of vortices by nanoprecipitates.

For the dense and strong pinning nanostructures of the samples studied here, pinning defects can also change the global electronic properties of the conductor, particularly the effective anisotropy parameter γ_{eff} due to strains around oxide nanoprecipitates, buckling of the ab planes, crystal mosaicity, and low-angle grain boundaries caused by dense pinning nanostructure result in local variations of the orientation of the c -axis with respect to the applied field. Also the local mass anisotropy ratio in the cuprates can change if defects cause local nonstoichiometry variations increasing $\gamma(\mathbf{r})$ in underdoped regions.

For instance, in the presence of a distribution of local orientations of the c -axis on scales greater than the coherence length, the global irreversibility field B_{Irr} is given by averaging the local relation Eq.

(1)

$$B_{Irr} = B_{max} \int_0^{\pi} \frac{F(\phi) d\phi}{\sqrt{\sin^2 \phi + \gamma^2 \cos^2 \phi}} \quad (3)$$

where $F(\phi)$ is the distribution function of the angles $\phi(\mathbf{r})$ between the local orientation of the c -axis and

the direction of the applied field, $F(\phi)$ is normalized by the condition $\int_0^{\pi} F(\phi) d\phi = 1$. The global

irreversibility field $B_{Irr}(\theta)$ can be for instance calculated for a narrow step-wise distribution $F(\phi) =$

$1/2\theta_0$ for $|\phi-\theta| < \theta_0$ and $F(\phi)=0$ for $|\phi-\theta| > \theta_0$ where θ_0 quantifies the spread of the local c -axis orientations

around the angle θ between \mathbf{B} and the mean orientation of the c -axis. For $\theta_0 \ll 1$ the parameter γ_{eff} ,

defined as $B_{Irr}(\pi/2)/B_{Irr}(0)$, decreases as θ_0 increases as shown in Fig. 7. However in this example the

reduction of γ from 5 to the observed ≈ 3 corresponds to $\theta_0 \approx 30^\circ$. Such a large angular spread of

misorientation angles suggests that this cannot be the only mechanism reducing γ . Another

characteristic feature of samples with a large content of nanoparticles is that the REBCO lattice is

buckled around pinning nanoparticles modulating the distance between the ab planes. In turn, a local

reduction of the ab distances due to strains might reduce the suppression of the order parameter

between the planes and decrease the effective mass anisotropy.

B. Correlated pinning

The ab peak in the 5%Zr-REBCO appears to have a single Lorentzian structure [Fig. 4(b)] in the temperature and field range of our measurements even if, because the magnitude of B_{Irr} becomes higher than 45 T, the full angular dependence of the ab peak was not measured. This single-peak structure is consistent with our TEM images (Fig. 1), showing a high density of stacking fault unevenly spaced by

distances $d_s \sim 10$ nm along the c -axis but no significant arrangement of the nanoprecipitates along the ab direction. Because of the short c -axis coherence length $\xi_c \sim 0.3-0.5$ nm in REBCO, stacking faults locally depress superconductivity, resulting in strong core and magnetic pinning of parallel vortices. For fields lower than the matching field, $B < B_s \sim \phi_0 / \gamma d_s^2 \approx 4$ T at $\gamma = 5$, vortex cores are mostly trapped by the stacking faults, so misalignment of B with the stacking faults causes a cusp-like drop of the pinning force,⁵ which manifests itself in the ab peak in B_{Irr} . For $B > B_s$ vortices also appear between the stacking faults which cut off currents circulating around vortices because $d_s \sim 10$ nm is much smaller than the London penetration depth $\lambda(77K) \approx 400$ nm along the c -axis. This results in strong magnetic pinning of vortices if the Josephson critical current densities across the stacking faults are smaller than $J_s \sim J_d \xi_c / d_s$ where J_d is the depairing current density in the ab plane.¹² In this case stacking faults effectively subdivide REBCO films into a stack of weakly coupled layers of different thickness distributed around ~ 10 nm $\ll \lambda(77K)$ which would result in a cusp-like peak in J_c , manifesting itself in the ab peak in B_{Irr} . Such strong cusps in J_c were indeed observed even for isotropic NbTi films in which the ab peak in J_c not only reached $\sim (0.1-0.2)J_d$ for a thin film with $d = \lambda/2$ but remained quite noticeable even for thicker films with $d = 2\lambda$.¹³ These results suggest that the long-range magnetic pinning of vortices by the sample surfaces could be essential for our REBCO films given that the thicknesses of 5%Zr-REBCO film (0.5 μm) and 10%Zr-REBCO film (1 μm) are both comparable to $\lambda(77K) \sim 0.4$ μm , thus, the thickness effect could contribute to the ab peaks in B_{Irr} . As is clear from Figs. 2(b) and 4(b), in this case the correlated pinning may enhance B_{Irr} parallel to the ab planes by as much as 50-100%, depending on temperature.

In the case of 10%Zr-REBCO, the double structure of the ab peak in B_{Irr} observed in Figs. 4(a) and 5 suggests that the peak may be determined by a superposition of different pinning mechanisms that can be roughly described by two Lorentz distributions in $\Delta B_{Irr}(\theta)$. The wider Lorentz peak in $\Delta B_{Irr}(\theta)$

exists at all temperatures and is shifted by $2-3^\circ$ with respect to the maximum of the RP contribution. Although several possible mechanisms (such as pinning by stacking faults and by film surface) may contribute to the broad peak in $\Delta B_{Irr}(\theta)$, the $2-3^\circ$ shift suggests also the influence of pinning by RE_2O_3 precipitates that in this sample grow in the ab planes but stack in a slightly tilted staircase manner, as observed in these same materials by Zhang *et al.*¹¹ and in similar materials by Holesinger *et al.*¹⁴

A distinctive feature of the 10%Zr-REBCO film is the emergence of an intense narrow ab peak in $\Delta B_{Irr}(\theta)$ as the temperature is decreased. A similar strong increase of B_{Irr} for B along the ab planes was first observed in underdoped YBCO crystals⁸ and later also in optimally doped YBCO films.⁹ In both cases the authors found that there is a characteristic temperature T_{cf} below which B_{Irr} increases very steeply with decreasing temperature for the field parallel to the ab planes. This characteristic temperature was estimated to be about 80K for the optimally doped YBCO.⁹ Gordeev *et al.*⁸ suggested that the vortex core diameter $2\xi_c$ becomes smaller than the separation of CuO planes below T_{cf} , leading to confinement of vortices between them. In this scenario the vortex liquid freezes below T_{cf} in a smectic phase in which the vortex confinement suppresses thermal fluctuation perpendicular to the CuO layers, while exerting no restraint within the layers, thus inducing crystalline order along the c -axis, while remaining liquid within the plane. Despite the strong ab peak in $\Delta B_{Irr}(\theta)$ in our sample that appears at about the same temperature observed by Baily *et al.*, we have to take into account the fact that in Ref. 9 a thin film with $d=0.2\lambda(77\text{K})$ and $\gamma=6$ was investigated. Our disordered and thicker REBCO samples appear to have lower anisotropy ~ 3 that, if related to a suppressed mass anisotropy, should weaken the intrinsic pinning by the ab planes. Yet the observed sudden increase of $\Delta B_{Irr}(\theta)$ at low temperature may suggest matching of the vortex core diameter $2\xi_c$ to the thickness of planar pinning defects in the sample. Indeed, stacking faults would be the most likely source of such narrow

ab peaks in $\Delta B_{Irr}(\theta)$ because the disruption of the natural sequence of the atomic planes along the c -axis and the short ξ_c make the stacking faults much stronger pins than the ab planes.

To further address the different nature of the narrow and the wide ab peaks in $\Delta B_{Irr}(\theta)$ shown in Fig. 5, we also studied the behavior of resistivity $\rho(B)$ near the depinning transition in which $\rho(B)$ is usually described by the equation $\rho \propto (B - B_{Irr})^s$, where the exponent s determines the shape of the resistive transition. Because in this equation a small change of B_{Irr} significantly affects the estimation of s , B_{Irr} was extracted independently from the intercept of the linear fit of $\rho \left[\frac{d\rho}{dB} \right]^{-1}$, as suggested in Ref.15, and the ρ - B curves were fitted by the power law equation with B_{Irr} fixed. As shown in Fig. 8, the mean value of s is about 3.3 ± 0.2 over almost the whole angular range, except for a small region close to $B//ab$, where s decreases to 1.4. Because such reduction of s is related to core pinning by planar defects, its effectiveness is inherently limited to the small angular region. When the angle between B and ab exceeds a few degrees, the vortices form kinked structures which are less strongly pinned than straight vortices parallel to the planar pinning defects.

For the field oriented away from the ab planes $s \approx 3.3$ is substantially lower than the 5.3 value found in a proton-irradiated single crystal,¹⁵ where a vortex glass phase is induced by isotropic random point defects. However, $s=3.3$ is similar to the results obtained by Baily *et al.*⁹ and Miura *et al.*¹⁰ for strong pinning REBCO films. Moreover, Fig. 8 also does not show any significant change in s close to $B//c$, where B_{Irr} is affected by the BZO nanorods.

Now we turn to the c -axis peak in $\Delta B_{Irr}(\theta)$ shown in Figs. 4(b) and 6. Here the splayed BZO nanorods result in a broad c -axis peak in $\Delta B_{Irr}(\theta)$ and apparently flatten the angular dependence of B_{Irr} over a wide region around the c -axis. This flattening is more evident at high temperature so that the magnitude of the c -axis peak normalized to the RP contribution $\Delta B_{Irr}(\theta)/B_{Irr,RP}(\theta)$ decreases as

temperature decreases, as shown in Fig. 6. Moreover, the peak in B_{Irr} is not at 180° but at about 190° , which is correlated to the splayed distribution of nanorod orientations shown in Fig. 1. The decreasing relative contribution of the c -axis peak at low temperature is at a first sight counterintuitive, because thermal wandering of vortices diminishes upon decreasing temperature and pinning by nanorods becomes stronger.¹⁶ Yet the increase of the ratio $\Delta B_{Irr}(\theta)/B_{Irr,RP}(\theta)$ at higher temperatures clearly indicates that thermal fluctuations suppress the random component $B_{Irr,RP}(\theta)$ more strongly than the correlated contribution $\Delta B_{Irr}(\theta)$. This effect can be explained by the influence of splayed nanorods which suppress thermal wandering of vortices by blocking proliferation of vortex kinks along the nanorods, thus reducing the effect of thermal fluctuations on ΔB_{Irr} as compared to the stronger suppression of $B_{Irr,RP}$. This scenario is based on the model proposed by Hwa *et al.*¹⁷ which has been used successfully to explain the strong reduction of flux creep and enhancement of B_{Irr} by splayed columnar defects produced by heavy ion irradiation of the cuprate single crystals.¹⁸ Extensive characterizations of the pinning of BZO-containing and BZO-free variants of these same samples have recently been made.^{19,20} Consistent with what found in the present paper, it has been concluded that the correlated pinning due to the BZO nanorods that strongly affect REBCO properties at high temperature becomes weak at low temperature. In fact it has been shown that the angular dependence of $J_c(4.2K)$ exhibits no sign of the c -axis peak and the RP contribution dominates. Because the thermal fluctuations are negligible at low temperature, the nanorods may act as effective pins also with a strongly misaligned field and they behave in a more isotropic way.

IV. CONCLUSIONS

We reported systematic studies of the anisotropic irreversibility fields of high-performance thin films with strong pinning nanostructures in very high fields up 45 T. By deconvoluting the RP from the correlated pinning contributions, we found that the former exhibits an effective anisotropy parameter

$\gamma_{RP} \sim 3$ rather than $\gamma = 5-6$ characteristic of the mass anisotropy in pure YBCO.^{9,10} Moreover, $B_{Irr}(\theta)$ is significantly affected by correlated pinning, which shows interesting temperature dependences, for field both along the ab and c directions. Correlated pinning for fields aligned close to the ab plane is able to nearly double the irreversibility field ($\Delta B_{Irr} \sim 25T$ at 78K). At high temperatures the peak in B_{Irr} is determined by magnetic pinning and is slightly affected by a tilt bias in the stacking of ab -planar RE_2O_3 precipitates,^{11,14} whereas below 80 K a significant contribution comes from the vortex core pinning by the stacking faults. The analysis of critical exponents at the depinning transition shows that this last mechanism is effective only in a very narrow region of angles and it becomes negligible once the field is tilted more than 2° away from the ab planes. By contrast, at the other field configurations s is 3.3 despite the presence of the BZO nanorods near the c -axis. This finding suggests that at 78K the contribution to B_{Irr} of correlated pinning along the BZO nanorods is already significantly reduced in favor of a more isotropic RP. For field along the c -axis, B_{Irr} is enhanced by $\sim 35\%$ at high temperature but this enhancement loses effectiveness rapidly at lower temperatures, decreasing to $\sim 14\%$ at 56K. Moreover, J_c measurements on similar samples have shown that the nanorods become less effective at 4.2 K both at high and low fields.^{19,20} This behavior suggests that nanorods act as correlated pins at high temperature but behave more like random pins at lower temperatures. This phenomenon indicates that the splay distribution of BZO nanorods effectively enhances the correlated pinning contribution to B_{Irr} by suppressing thermal wandering of vortices close to T_c .

A portion of this work was performed at the NHMFL, which is supported by NSF Cooperative Agreement No. DMR-0654118, by the State of Florida, and by the DOE. This work was also supported by the U.S. Department of Energy Office of Electricity Delivery and Energy Reliability, Advanced Cables and Conductors.

APPENDIX

The angular dependence of the global irreversibility field $B_{Irr}(\theta)$ can be calculated for a narrow step-wise distribution $F(\phi) = 1/2\theta_0$ for $|\phi - \theta| < \theta_0$ and $F(\phi) = 0$ for $|\phi - \theta| > \theta_0$ where θ_0 quantifies the spread of the local c -axis orientations around the angle θ between \mathbf{B} and the mean orientation of the c -axis. For $\theta_0 \ll 1$ but $\gamma\theta_0 > 1$, the distribution of the c -axis misorientations can affect the angular dependence of B_{Irr} . In this case $\cos\phi$ and $\sin\phi$ in Eq. (3) can be expanded around the point $\phi = \theta$ up to quadratic terms in $u = \phi - \theta$, which gives after integration:

$$B_{Irr} = \frac{B_{max}}{2\theta_0 |(\gamma^2 - 1)\cos 2\theta|^{1/2}} \left[\sin^{-1} \frac{\sin 2\theta + 2\theta_0 \cos 2\theta}{|1 + \cos^2 2\theta + 2\alpha \cos 2\theta|^{1/2}} - \sin^{-1} \frac{\sin 2\theta - 2\theta_0 \cos 2\theta}{|1 + \cos^2 2\theta + 2\alpha \cos 2\theta|^{1/2}} \right], \quad 0 \leq \theta \leq \pi/4 \quad (A1)$$

$$B_{Irr} = \frac{B_{max}}{2\theta_0 |(\gamma^2 - 1)\cos 2\theta|^{1/2}} \left[\sinh^{-1} \frac{\sin 2\theta - 2\theta_0 \cos 2\theta}{|1 + \cos^2 2\theta + 2\alpha \cos 2\theta|^{1/2}} - \sinh^{-1} \frac{\sin 2\theta + 2\theta_0 \cos 2\theta}{|1 + \cos^2 2\theta + 2\alpha \cos 2\theta|^{1/2}} \right], \quad \pi/4 \leq \theta \leq \pi/2$$

where $\alpha = (\gamma^2 + 1)/(\gamma^2 - 1)$. The effective anisotropy factor $\gamma_{eff} = B_{Irr}(\pi/2)/B_{Irr}(0)$ obtained from Eq. (A1) results in

$$\gamma_{eff} = \frac{\sinh^{-1}(\theta_0 \sqrt{\gamma^2 - 1})}{\sin^{-1}[(\theta_0 \sqrt{\gamma^2 - 1})/\gamma]} \quad (A2)$$

And γ_{eff} as a function of θ_0 is shown in Fig. 7.

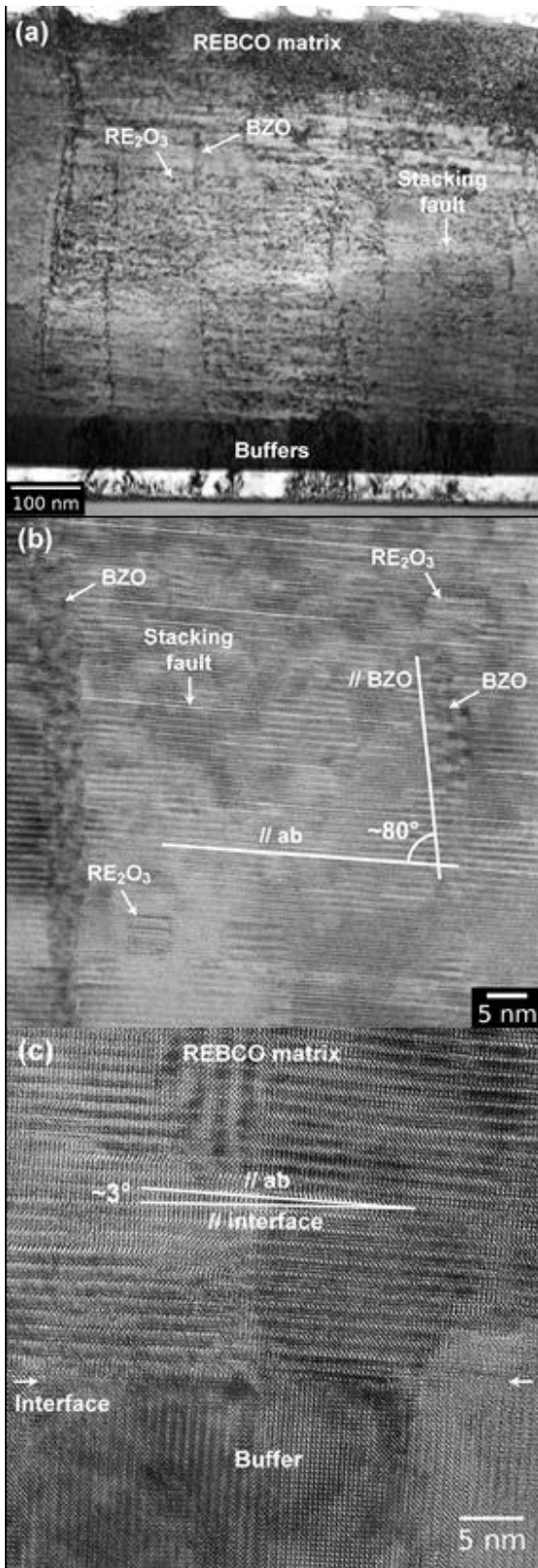


Fig. 1 Transverse cross-sectional TEM images of the 5%Zr-REBCO sample showing (a) three types of pinning defects: BZO nanorods, RE_2O_3 nano-precipitates and stacking faults, (b) the average angle of $\sim 80^\circ$ between the direction of nanorods and the REBCO *ab*-plane, (c) the REBCO *ab* planes tilted $\sim 3^\circ$ from the buffer interface.

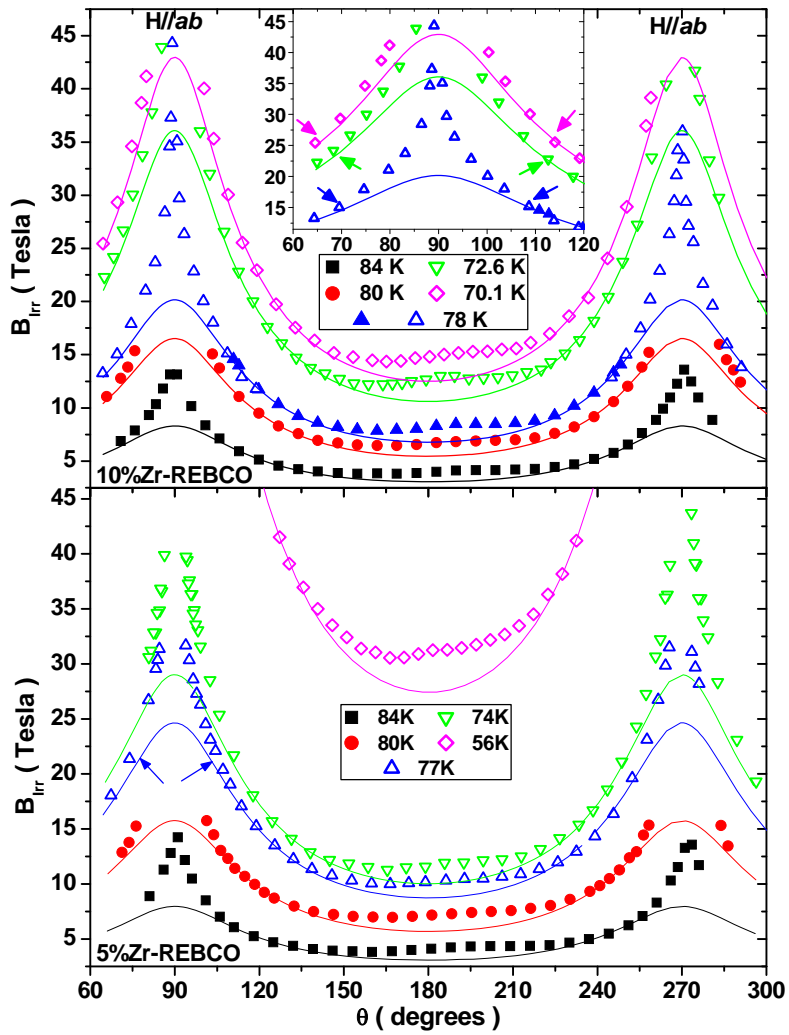


Fig. 2 Angular dependences of the irreversibility field B_{Irr} (symbols) for a 10%Zr and 5%Zr-REBCO samples and random pinning contribution $B_{Irr,RP}$ to B_{Irr} (lines), determined as explained in the text. In the inset, magnification close to 90° for the 10%Zr-REBCO.

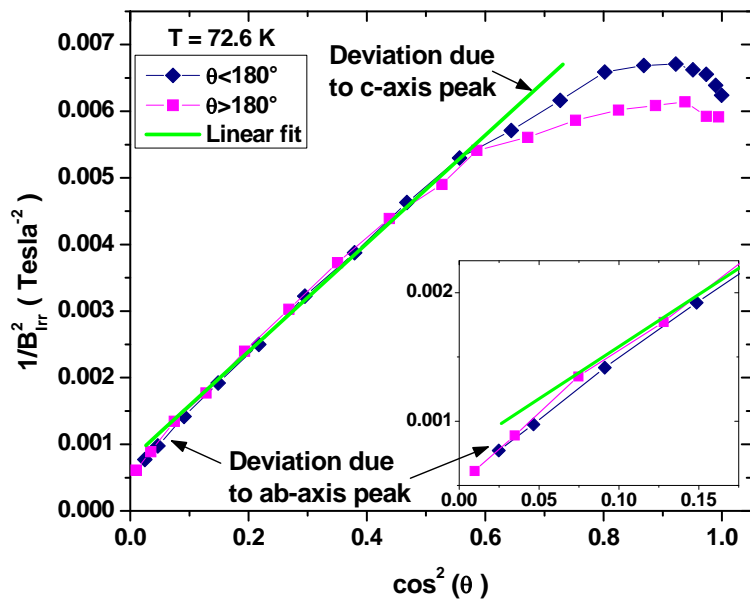


Fig. 3 B_{irr} data from Fig. 2 at 72.6 K, replotted as $1/B_{irr}^2$ versus $\cos^2(\theta)$ and magnification close to zero in the inset.

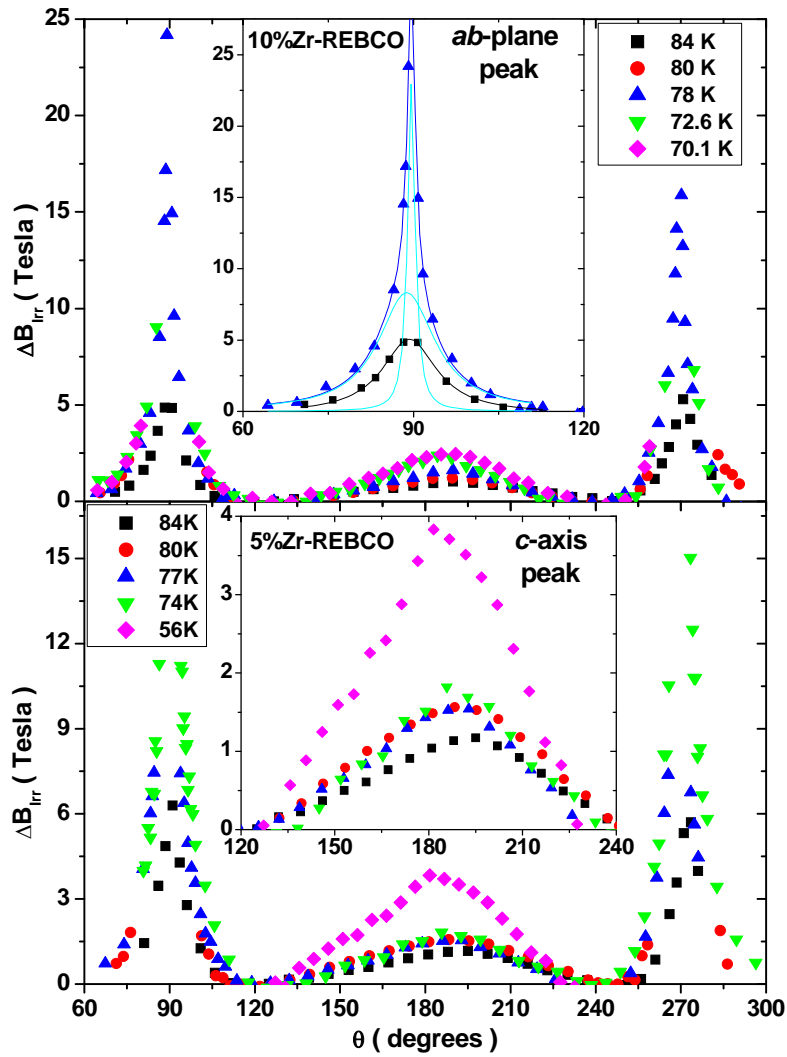


Fig. 4 Correlated pinning contributions ΔB_{irr} , determined by subtracting the RP contribution from the experimental data of Fig.2. Inset of (a) shows the single and double peak fits at 84 and 78K, respectively, of the correlated pinning along ab for the 10%Zr-REBCO sample. Inset of (b) shows an expanded view of the c -axis peak for the 5%Zr-REBCO sample.

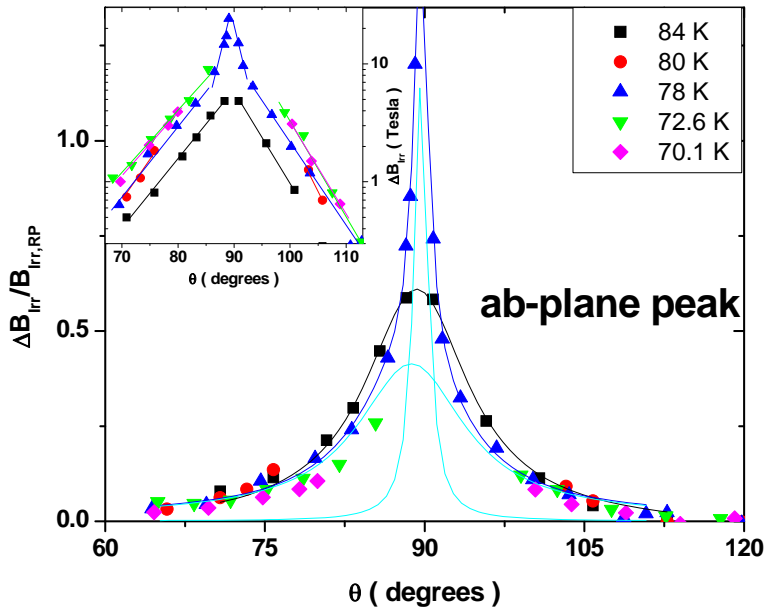


Fig. 5 Correlated pinning contributions along the *ab* plane plotted on a logarithmic scale, showing the dependence of single- and double-peak structures on temperature.

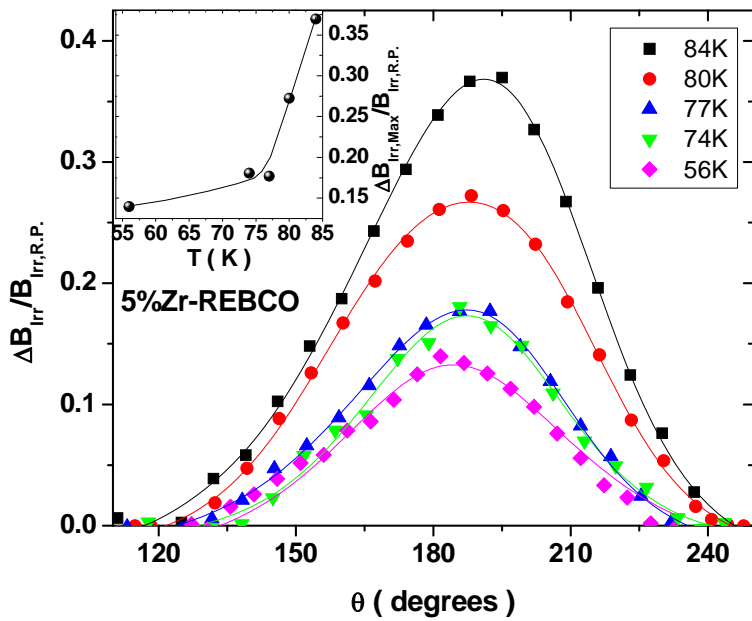


Fig. 6 Correlated pinning contributions normalized to the RP one close to the *c*-axis; the inset shows the temperature dependence of the peak maxima.

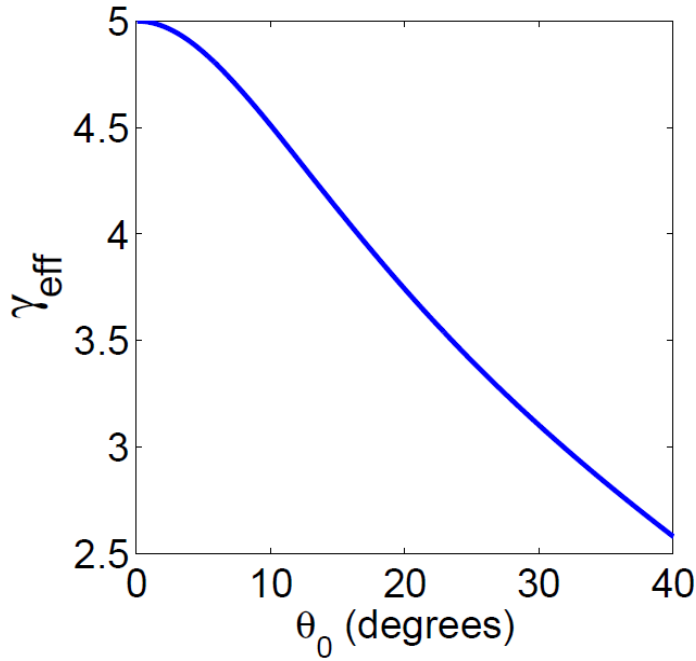


Fig. 7 Dependence of the effective anisotropy parameter γ_{eff} on the width of the c-axis distribution θ_0 defined by Eq. (4) for $\gamma = 5$.

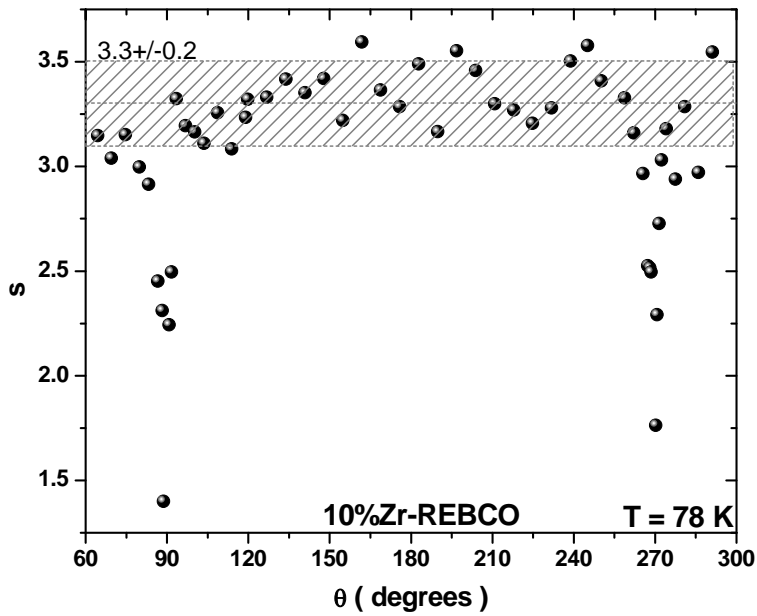


Fig. 8 Critical exponent s , determined from the transition fits with $\rho \propto (B - B_{\text{irr}})^s$, as a function of angle. The shaded area represents the spread around the mean value over the entire range.

References

- ¹ X. Song, Z. Chen, S.I. Kim, D.M. Feldmann, D.C. Larbalestier, J. Reeves, Y. Xie, and V. Selvamanickam, *Appl. Phys. Lett.* **88**, 212508 (2006); L. Stan, T.G. Holesinger, B. Maiorov, Y. Chen, D.M. Feldmann, I.O. Usov, R.F. DePaula, V. Selvamanickam, L. Civale, S.R. Foltyn, Q.X. Jia, *Supercond. Sci. Technol.* **21**, 105023 (2008)
- ² Z. Chen, D.M. Feldmann, X. Song, S.I. Kim, A. Gurevich, J. Reeves, Y. Xie, V. Selvamanickam, and D.C. Larbalestier, *Supercond. Sci. Technol.* **20**, S205 (2007)
- ³ Y. Chen, V. Selvamanickam, Y. Zhang, Y. Zuev, C. Cantoni, E. Specht, M.P. Paranthaman, T. Aytug, A. Goyal, D. Lee, *Appl. Phys. Lett.* **94**, 062513 (2009).
- ⁴ J.L. MacManus-Driscoll, S.R. Foltyn, Q.X. Jia, H. Wang, A. Serquis, L. Civale, B. Maiorov, M.E. Hawley, M.P. Maley, and D.E. Peterson, *Nat. Mater.* **3**, 439 (2004); S. Kang, A. Goyal, J. Li, A. A. Gapud, P. M. Martin, L. Heatherly, J. R. Thompson, D. K. Christen, F. A. List, M. Paranthaman, and D. F. Lee, *Science* **311**, 1911 (2006); B. Maiorov, S. A. Baily, H. Zhou, O. Ugurlu, J. A. Kennison, P. C. Dowden, T. G. Holesinger, S. R. Foltyn and L. Civale, *Nat. Mater.* **8**, 398(2009).
- ⁵ G. Blatter, V.B. Geshkenbein, A.I. Larkin, *Phys. Rev. Lett.* **68**, 875 (1992).
- ⁶ L. Civale, B. Maiorov, A. Serquis, J. O. Willis, J. Y. Coulter, H. Wang, Q.X. Jia, P. N. Arendt, J. L. Manus-Driscoll, M. P. Maley, and S. R. Foltyn, *Appl. Phys. Lett.* **84**, 2121 (2004); J. Gutierrez, A. Llordes, J. Gazquez, M. Gibert, N. Roma, S. Ricart, A. Pomar, F. Sandiumenge, N. Mestres, T. Puig, and X. Obradors, *Nat. Mater.* **6**, 367 (2007).
- ⁷ L. Civale *et al* *J. Low Temp. Phys.* **135**, 87 (2004)
- ⁸ S. N. Gordeev, A. A. Zhukov, P. A. J. de Groot, A. G. M. Jansen, R. Gagnon, and L. Taillefer, *Phys. Rev. Lett.* **85**, 4594 (2000).
- ⁹ S. A. Baily, B. Maiorov, H. Zhou, F. F. Balakirev, M. Jaime, S. R. Foltyn, and L. Civale, *Phys. Rev. Lett.* **100**, 027004 (2008).
- ¹⁰ M. Miura, S. A. Baily, B. Maiorov, L. Civale, J. O. Willis, K. Marken, T. Izumi, K. Tanabe, and Y. Shiohara, *Appl. Phys. Lett.* **96**, 072506 (2010).
- ¹¹ Y. Zhang, E.D. Specht, C. Cantoni, D.K. Christen, J.R. Thompson, J.W. Sinclair, A. Goyal, Y.L. Zuev, T. Aytug, M.P. Paranthaman, Y. Chen, V. Selvamanickam, *Physica C* **469**, 2044 (2009).
- ¹² A. Gurevich and L.D. Cooley, *Phys. Rev. B* **50**, 13563 (1994).
- ¹³ G. Stejic, A. Gurevich, E. Kadyrov, D. Christen, R. Joynt, and D.C. Larbalestier, *Phys. Rev. B* **49**, 1274 (1994).
- ¹⁴ T. G. Holesinger, B. Maiorov, O. Ugurlu, L. Civale, Y. Chen, X. Xiong, Y. Xie and V. Selvamanickam, *Supercond. Sci. Technol.* **22**, 045025 (2009).
- ¹⁵ A. M. Petrean, L. M. Paulius, W.-K. Kwok, J. A. Fendrich, and G.W. Crabtree, *Phys. Rev. Lett.* **84**, 5852 (2000).
- ¹⁶ D.R. Nelson and V.M. Vinokur, *Phys. Rev. B* **48**, 13060 (1993).
- ¹⁷ T. Hwa, P. LeDoussal, D.R. Nelson and V.M. Vinokur, *Phys. Rev. Lett.* **71**, 3545 (1993).
- ¹⁸ L. Civale, *Supercond. Sci. Technol.* **10**, A11 (1997).
- ¹⁹ A. Xu, J.J. Jaroszynski, F. Kametani, Z. Chen, D.C. Larbalestier, Y.L. Viouchkov, Y. Chen, Y. Xie and V. Selvamanickam, *Supercond. Sci. Technol.* **23**, 014003 (2010)
- ²⁰ V. Braccini, A Xu, J. Jaroszynski, Y. Xin, D.C. Larbalestier, Y. Chen, G. Carota, J. Dackow, I. Kesgin, Y. Yao, A. Guevara, T. Shi, V. Selvamanickam, *Supercond. Sci. Technol.* **24**, 035001 (2011)